Quantum oscillations and quasilinear magnetoresistance in the topological semimetal candidate $ScSn_2$

Y. Chen,[1,*] F. Tang,[1,2,*] W. Z. Meng,[3] X. Shen,[1] W. Zhao,[4] X. Q. Yin,[5,6] S. Cong,[1] Q. H. Yi,[1] L. Zhang,[1] D. J. Wu,[1] Z.-D. Han,[1] B. Qian,[1,†] X.-F. Jiang,[1] X. M. Zhang,[3,‡] and Y. Fang[1,§]

[1]*Jiangsu Laboratory of Advanced Functional Materials, Department of Physics, Changshu Institute of Technology, Changshu 215500, China*
[2]*Jiangsu Key Laboratory of Thin Films, School of Physical Science and Technology, Soochow University, Suzhou 215006, China*
[3]*School of Materials Science and Engineering, Hebei University of Technology, Tianjin 300130, China*
[4]*ISEM, Innovation Campus, University of Wollongong, Wollongong, New South Wales 2500, Australia*
[5]*Joint Key Laboratory of the Ministry of Education, Institute of Applied Physics and Materials Engineering, University of Macau, Avenida da Universidade, Taipa, Macau SAR 999078, China*
[6]*Key Laboratory of Artificial Structures and Quantum Control (Ministry of Education), Shenyang National Laboratory for Materials Science, School of Physics and Astronomy and Tsung-Dao Lee Institute, Shanghai Jiao Tong University, Shanghai 200240, China*

(Received 27 May 2021; accepted 5 October 2021; published 15 October 2021)

Novel compounds with two-dimensional square lattices formed by group IV or V elements (Si, Sn, Ge, Bi, and Sb) have been attracting a great deal of attention in recent times, mainly because of the possible emergence of various topological phases therein. Here, we successfully grow the single crystals of Sn-square-net based material $ScSn_2$, and systematically perform their magnetization and magnetotransport measurements. Clear quantum oscillations emerge in the magnetization isotherms along different field orientations, from which nonzero Berry phases are extracted, implying that $ScSn_2$ harbors three-dimensional Fermi surfaces and nontrivial electronic states. Similar to many other topological semimetals with extremely large magnetoresistance, $ScSn_2$ shows field-induced resistivity enhancement as well, which has been proven to be not of a gap opening origin. Besides, at low temperature, large magnetoresistance with a quasilinear field dependence is observed. Our analysis of the magnetotransport data finds that the quasilinear magnetoresistance in $ScSn_2$ cannot be understood by several familiar mechanisms proposed in the literature. These findings are expected to have far reaching implications for both the fundamental understanding and magnetoresistance device application of topological semimetal materials.

DOI: 10.1103/PhysRevB.104.165128

I. INTRODUCTION

Topological semimetals are currently a new frontier and focus topic in physics and materials science communities for their unique physical properties governed by the underlying topology of electronic states and potential applications in high-efficiency spintronic and quantum computing devices [1,2]. Featured by the degeneracy and distribution of band-crossing points in the Brillouin zone (BZ), and associated topological boundary states, nontrivial semimetals can be simply classified into Dirac, Weyl, and nodal-line ones [1,2]. To date, a variety of topological semimetal candidates have been theoretically proposed and experimentally confirmed [3–19]. Among them, one class of materials, which feature the layered structures composed by group IV or V elements such as Si, Sn, Ge, Bi, and Sb, are of great interest for their plentiful topological states. The examples include $AMnPn_2$– (A = Ca, Sr, Ba, Eu, Yb; Pn = Sb, Bi) [9–15], WHM- (W = Zr, Hf, or rare-earth elements; H = Si, Ge, Sn, Sb; M = S, Se, Te) [16–19] and $AZnPn_2$-type (A = Sr, Ba, Eu; Pn = Sb, Bi) compounds [19–22]. A large pool of topological electronic phases, like anisotropic Dirac cone states, nodal-line states, two-dimensional (2D) nonsymmorphic Dirac states, time-reversal symmetry breaking type-II Weyl states, and so on [18,19], are created in the 2D square lattices or distorted square lattices. Thus, materials featuring the structural motif of a square net can provide a fertile ground for developing diverse topological states.

Here, we focus on $ScSn_2$ that belongs to a large family of rare-earth distannides RSn_2 and is predicted to be a potential topological semimetal [19,23]. As shown in Fig. 1(a), $ScSn_2$ crystallizes in a tetragonal structure with the space group I_{41}/amd, and is built up from an alternate stacking of the trigonal prism-type Sc slabs centered by Sn atoms and Sn layers, along the c axis [23]. Note that the Sn planar layer is a square net with all the bonding angles being of 90° and thus this plane is exactly 2D [23]. A different case is found in YSn_2. Zhu *et al.* reveal that this compound crystallizes in a crystal structure with the $Cmc2_1$ space group and lightly distorted Sn square lattice [24]. What's more, a tunable Weyl state and a quasi-2D band are found in this compound [24]. Given the structural diversity of the RSn_2 series [25], different electronic states could

*These authors contributed equally to this work.
†njqb@cslg.edu.cn
‡zhangxiaoming87@hebut.edu.cn
§fangyong@cslg.edu.cn

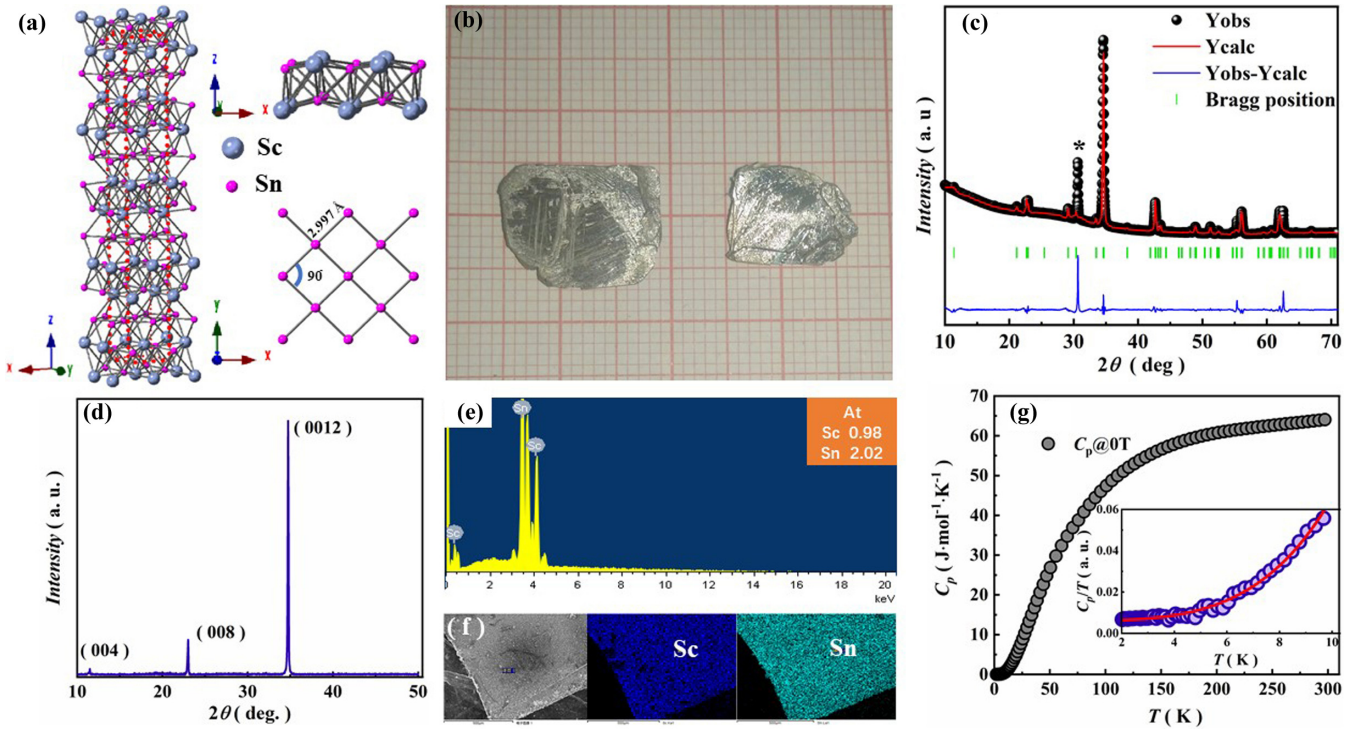

FIG. 1. (a) Crystallographic structure of $ScSn_2$, a trigonal prism-type Sc slab centered by Sn atoms and a Sn layer. (b) Photographs of synthesized single-crystal $ScSn_2$ placed on a millimeter grid. (c) Powder XRD results (black solid sphere) at room T. The red line is the best fit from the Rietveld refinement using FULLPROF software. Small amount of residual Sn flux (marked with a black asterisk) is present in the x-ray pattern (d) XRD patterns with the x rays along the perpendicular direction of crystal surfaces. (e) EDX for $ScSn_2$ crystals. (f) A SEM image for $ScSn_2$ crystals and elemental distributions of Sc and Sn acquired by scanning EDX. (g) C_p vs T and C_p/T vs T (inset) plots for $ScSn_2$ crystals.

be expected in other members. Here, we grow $ScSn_2$ single crystals and study their electronic band structures, magnetization (M), magnetoresistance (MR), Hall resistivity (ρ_{xy}), and so on. Theoretical calculations suggest that this compound is a topological semimetal. This is confirmed by the nontrivial Berry phase (ϕ_B) extracted from M oscillations. Besides, magnetic-field (B) induced enhancement of resistivity (ρ_{xx}), and large quasilinear MR are observed at low temperature (T). We find that the large quasilinear MR in $ScSn_2$ could not be simply understood by reported mechanisms in the literature, and the actual cause to bring about such a situation is an open issue.

II. EXPERIMENTAL DETAILS

Growth of $ScSn_2$ single crystals was facilitated using the self-flux method. High-purity Sc (chunk, 99.9%) and Sn (powder, 99.999%) starting materials were carefully mixed in the atomic ratio of Sc : Sn = 1 : 9, placed in an alumina crucible, and encapsulated in an evacuated silica tube under partial pressure of Ar gas. The mixture was heated to 1073 K, maintained for 24 h, and then slowly cooled down to 673 K at a rate of 1 K/h. At this T, the excess Sn flux was removed by centrifugation, and then platelike crystals [see Fig. 1(b)] were obtained. Note that no sign of discernible surface oxidation was observed even if these crystals were exposed to air over a long period of time.

Crystal structure was confirmed by the x-ray diffraction (XRD) performed on a Rigaku D/Max-2200/PC diffractometer with Cu $Ka1$ radiation. Atomic proportion and elemental mapping were examined by a field-emission scanning electron microscope (FE-SEM, Zeiss Sigma) equipped with an Oxford Instruments INCA energy-dispersive x-ray (EDX) system.

Isothermal M was measured by a commercial Quantum Design magnetic property measurement system (MPMS-7). Specific heat (C_P) measurements were carried out by the adiabatic thermal relaxation method. ρ_{xx} and ρ_{xy} were measured by a conventional four-terminal technique. All these electrical and thermal property measurements were performed on a Quantum Design physical property measurement system (PPMS-9).

III. THEORETICAL DETAILS

First-principles band-structure calculations were performed based on the density functional theory (DFT) as implemented in the Vienna *ab-initio* simulation package [26,27]. The generalized gradient approximation of Perdew-Burke-Ernzerhof method was employed to describe exchange and correlation effects [28]. The cutoff value of plane wave kinetic energy was set as 400 eV, and the BZ was sampled with a 13 × 13 × 13 Γ-centered k-point mesh for structural optimization and self-consistent calculations. The energy convergence criteria were chosen to be less than 10^{-6} eV for electronic structures. Here, the DFT + U method was also adopted to calculate the band structures due to the contribution derived from the d orbitals of transition metal elements

TABLE I. Unit-cell parameters, reliability factors, and atomic positional parameters for $ScSn_2$.

Chemical formula	$ScSn_2$
Structure	tetragonal
Space group	I_{41}/amd
a (A°)	4.238(3)
b (A°)	4.238(3)
c (A°)	31.077 (3)
$\alpha = \beta = \gamma(^\circ)$	90
R_p (%)	3.36
R_{wp} (%)	7.84
R_{exp} (%)	2.99
χ^2	6.90
Sc (x, y, z)	(0.000 00, 0.250 00, 0.202 57)
Sn1 (x, y, z)	(0.000 00, 0.250 00, 0.034 01)
Sn2 (x, y, z)	(0.000 00, 0.250 00, 0.375 00)
Sn3 (x, y, z)	(0.000 00, 0.750 00, 0.125 00)

[29,30], where the effective U value for Sc atom was chosen as 3 eV.

IV. RESULTS AND DISCUSSION

Figure 1(c) shows the powder XRD patterns for $ScSn_2$ along with its Rietveld refinements performed using FULLPROF software [31]. As seen, all the diffraction peaks can be indexed to a tetragonal phase with the space group I_{41}/amd. Detailed structural parameters are given in Table I. Figure 1(d) depicts the XRD spectra for $ScSn_2$ single crystal, where only the $(00l)$ peaks are observed, suggesting that our crystals are of good quality with a preferential c-axis orientation. Besides, we have checked the chemical components of the as-prepared crystals by using the EDX measurements performed at different positions on the sample surfaces. As plotted in Fig. 1(e), the averaged Sc to Sn atom ratio is determined to be about 0.98:2.02, which is in good agreement with the stoichiometric ratio for $ScSn_2$. According to the EDX element mappings shown in Fig. 1(f), Sc and Sn are homogeneously distributed across the crystal surface, confirming the absence of Sn film or cluster therein. Figure 1(g) displays C_P as a function of T, where no anomalies hinting to a thermodynamic phase transition can be tracked. Generally, C_P at low T can be described using the formula $C_p = \gamma T + \beta T^3 + \delta T^5$ [32], where the first and two last terms are derived from the electron and lattice contributions, respectively. An analysis of C_P allows the determination of Sommerfeld coefficient (γ) and thus we show the C_p/T versus T plot with the red solid line denoting the best fitting to the experimental data [see the inset of Fig. 1(g)]. As depicted, a fit of these data in the T range 2–10 K yields $\gamma = 5.8\,\mathrm{mJ\,mol^{-1}\,K^{-2}}$. Note that this value is on the same order of magnitude as those reported for ZrSiS ($6.84\,\mathrm{mJ\,mol^{-1}\,K^{-2}}$) [33] and $YbMnBi_2$ ($2.16\,\mathrm{mJ\,mol^{-1}\,K^{-2}}$) [34], but much larger than that of the Weyl semimetal NbAs ($0.09\,\mathrm{mJ\,mol^{-1}\,K^{-2}}$) [35], suggesting that the density of state (DOS) around the Fermi level (FL) should not be negligible in the title compound.

To address the topological character of electronic band structures for $ScSn_2$, the *ab initio* DFT calculations with and without spin-orbit coupling (SOC) interactions are performed. Figure 2(a) shows the electronic band structures along the high-symmetry directions without considering the SOC effect, where the valence and conduction bands along the Y-Σ-Γ, X-Γ, and N-P paths highly intersect with each other, giving rise to six crossing points denoted as P_1, P_2, P_3, P_4, P_5, and P_6, respectively. Since $ScSn_2$ is nonmagnetic and crystallizes in a tetragonal structure with the space group I_{41}/amd [23], the time-reversal (T) and space-inversion (P) symmetries are preserved. Hence, in the absence of SOC, the above-mentioned band crossings should belong to several nodal loops instead of being discrete points [36]. It follows that the nodal lines are protected by the combination of P and T symmetries. This requires that ϕ_B along any close path in the system is quantized in units of π, which have been numerically verified by our calculation. Consequently, these nodal lines can't be gapped out by weak perturbations that preserve the PT symmetries. In Fig. 2(b), we find that the nodal lines for P_1–P_5 locate in the $k_z = 0$ plane and the nodal line around P_6 locates in the $k_x = 0$ plane. Our calculations show that the crossing bands have opposite $M_z(M_x)$ eigenvalues in the mirror-invariant planes. This suggests that the nodal lines are also protected by mirror symmetries. Thus, two independent protection mechanisms apply for the nodal lines in $ScSn_2$. As shown in Fig. 2(a), the band crossing points show no energy gaps, while, once the SOC is included, all the crossing points (nodal loops) are subtly altered [see Fig. 2(c)] and tiny gaps of 42, 0.8, 17.1, 128, and 33 meV are opened for P_1, P_2, P_4, P_5, and P_6, respectively. Note that the P_3 point composed of the p_y, p_z, d_{xz}, d_{xy} orbitals of the Sn atom [see Fig. 2(d)] hosts a SOC gap with a tiny value of ~0.3 meV that is much smaller than the bandwidth (~0.3 eV). In Fig. 2(c), the gap is located away from FL, implying that $ScSn_2$ could be regarded as a nodal-line semimetal [37]. Incidentally, the same issue (SOC opening a gap) also applies to other "Dirac" line-node semimetals like Ca_3P_2 [38], ZrSiM (M = S, Se, Te) [39], and Cu_3(Pd, Zn)N [40,41]. Note that similar to some other predicted nodal-line semimetals, including $PtSn_4$ [42,43], $CeCuBi_2$ [44,45], and Fe_2MnX (X = P, As, Sb) [46], $ScSn_2$ shows complex electronic band structures as well. Thus, we further check the reliability of its nodal-line electronic states (Fig. S1 in the Supplemental Material [47]).

Quantum oscillation, which is a result of singularity in DOS at the FL that occurs every time a Landau level (LL) crosses the FL [48], provides an effective way to capture the electronic characters of materials. Thus, we perform the out-of-plane ($B \parallel c$) and in-plane ($B \parallel ab$) isothermal M measurements up to 7 T for $ScSn_2$ at different Ts. As shown in Figs. 3(a) and 3(b), striking M oscillations are detected over a wide range of T from 1.8 to 12 K, revealing that the Fermi surface (FS) of $ScSn_2$ is 3D in nature. Besides, weak but detectable M oscillations can be tracked down to 0.6 T at 1.8 K, corresponding to a large magnetic length [$l_B = (\hbar/eB)^{1/2}$] of 33.49 nm, which again confirms that the as-grown $ScSn_2$ crystals are of high quality and indicates that the quasiparticles could host very low effective mass (m^*) and ultrahigh mobility (μ) [49]. Note that the M isotherm at 1.8 K deviates from those at other Ts in Figs. 3(a) and the background of M isotherms in Figs. 3(b) does not show a decrease above 8 K. These unexcepted behaviors may be

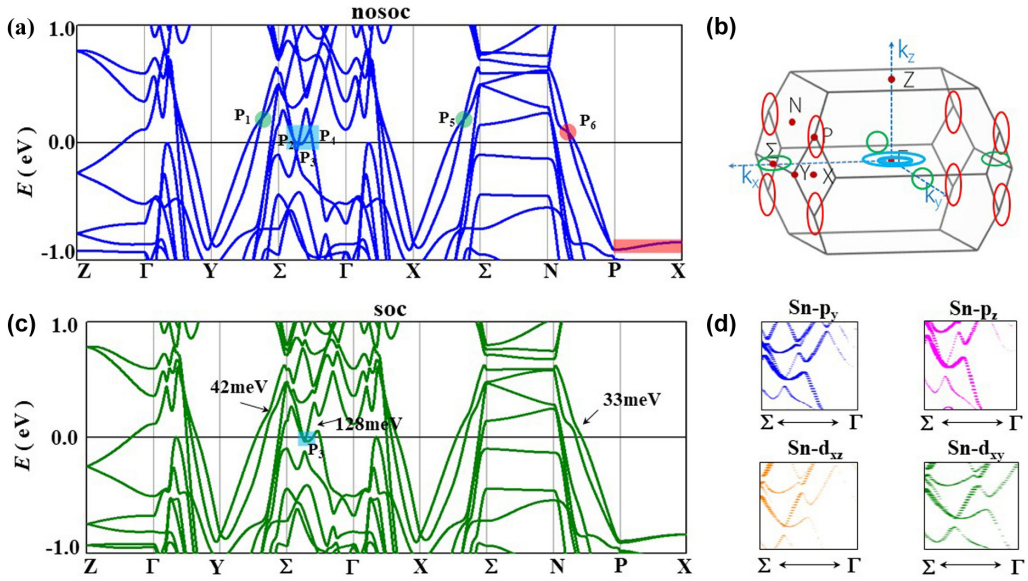

FIG. 2. (a) Electronic band structures for $ScSn_2$ without SOC, in which $P_1 - P_6$ denote the six crossing points near the FL, respectively. (b) Positions of the nodal loops in BZ. (c) Electronic band structures for $ScSn_2$ with SOC. Tiny gaps of 42, 0.8, 0.3, 17.1, 128, and 33 meV are opened for $P_1 - P_6$, respectively. (d) Contributions from Sn orbitals to P_3.

attributed to some magnetic impurities residing on the sample holders (quartz and brass rods equipped in MPMS-7). Figures 3(c) and 3(d) plot the oscillatory components of M (ΔM) for $B \parallel c$ and $B \parallel ab$ respectively, after a cautious subtraction of nonoscillatory and smooth backgrounds. It is clear that M oscillations decrease with the increasing T and decreasing B. Figures 3(e) and 3(f) show the fast Fourier transformation (FFT) spectra, from which the number and magnitude of all the frequencies (Fs) involved in the quantum oscillations can be extracted. As exhibited, a fundamental $F_\alpha = 21\,\mathrm{T}$ with its second harmonic $F_{2\alpha} = 42\,\mathrm{T}$ for $B \| c$, and $F_\beta = 32\,\mathrm{T}$ and $F_\gamma = 36.5\,\mathrm{T}$ for $B \parallel ab$ are observed. The presence of F_α, $F_{2\alpha}$, F_β, and F_γ is confirmed by fitting ΔM for $B \parallel c$ and $B \parallel ab$ with the multiband Lifshitz-Kosevish (LK) formula [insets

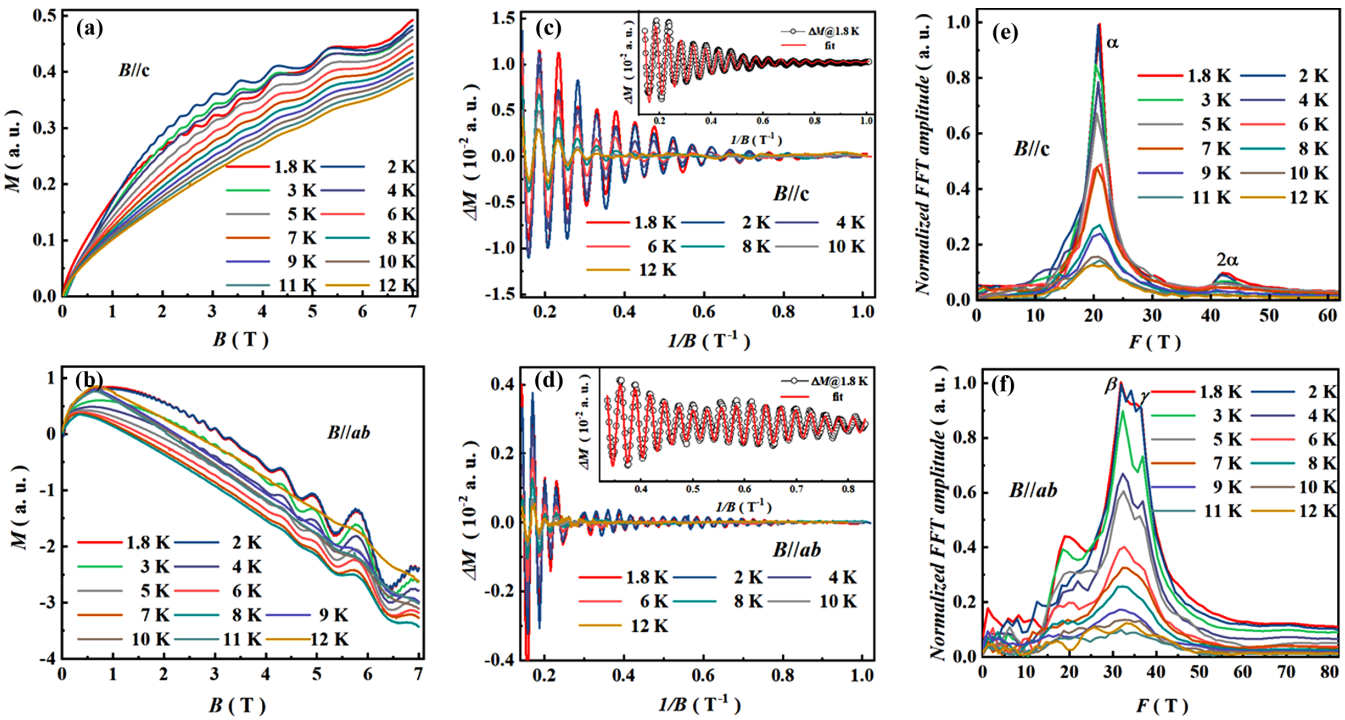

FIG. 3. (a),(b) M isotherms for $ScSn_2$ with $B \parallel a$ and $B \parallel ab$, respectively. (c),(d) ΔM vs $1/B$ for $B \parallel a$ and $B \parallel ab$, respectively. Insets show ΔM vs $1/B$ curves and their LK fittings at 1.8 K for $B \parallel c$ and $B \parallel ab$, respectively. (e),(f) FFT spectra of the out-of-plane (c) and in-plane (d) ΔM for $ScSn_2$ at various Ts.

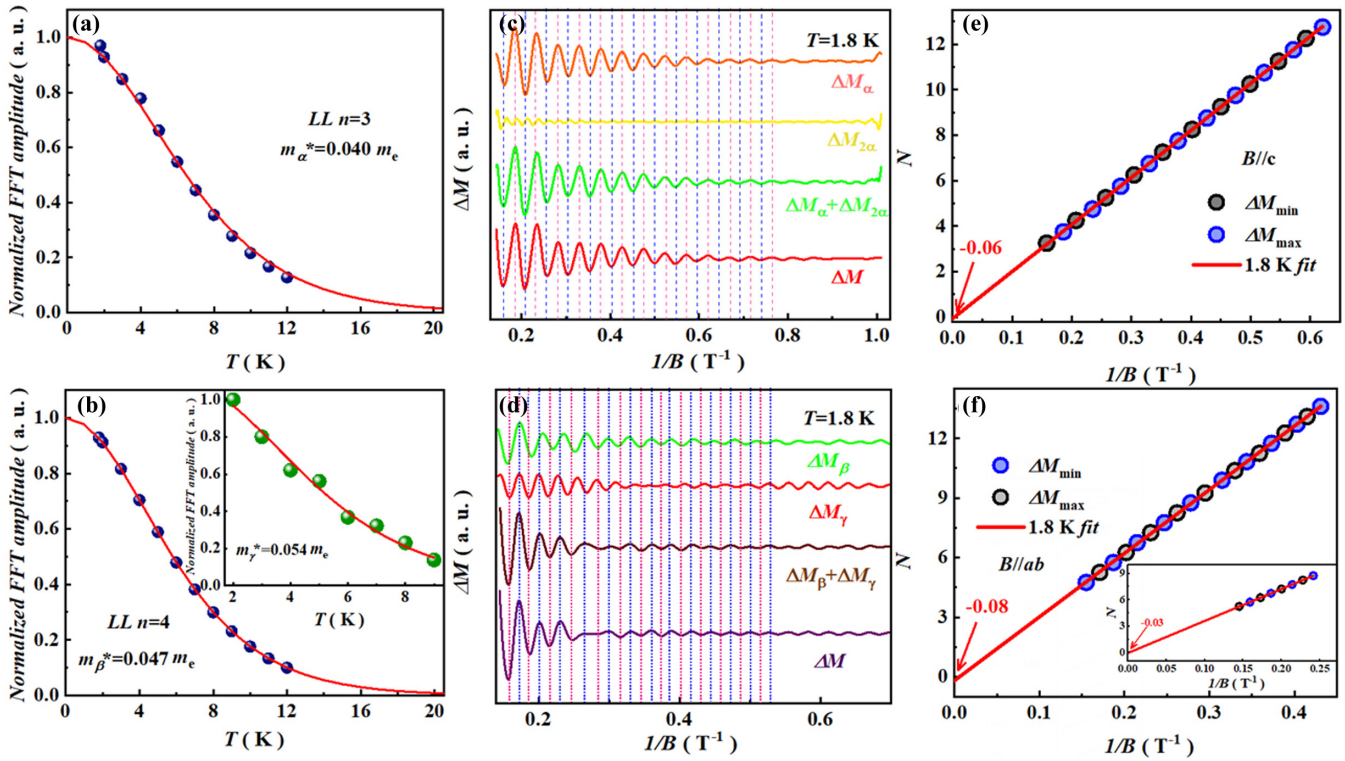

FIG. 4. (a), (b) T dependence of the out-of-plane ($B \parallel c$) and in-plane ($B \parallel ab$) normalized FFT amplitude for $ScSn_2$; the red solid lines represent the LK fit for $m_\alpha{}^*$, $m_\beta{}^*$, and $m_\gamma{}^*$. (c) ΔM_α, $\Delta M_{2\alpha}$, $\Delta M_\alpha + \Delta M_{2\alpha}$, and the experimental data ΔM for $B \parallel c$ vs $1/B$. (d) ΔM_β, ΔM_γ, $\Delta M_\beta + \Delta M_\gamma$, and the experimental data ΔM for $B \parallel ab$ vs $1/B$. (e), (f) LL index fan diagram for F_α, F_β, and F_γ. $N - 1/4$ and $N - 3/4$ (N, integer LL indices) are assigned to ΔM oscillation minima and maxima, respectively.

of Figs. 3(c) and 3(d)] [48]. The obtained Fs are far less than those reported for several other topological semimetals, including YSn_2 (78 T) [24], $LuSn_2$ (70 T) [49], Cd_3As_2 (58.3 T) [50], $PtBi_2$ (>250 T) [51], T_d-$MoTe_2$ (>226 T) [52], WP_2 (>1460 T) [53], and so on, which suggests that FS around the FL is small in the title compound. As known, an F in quantum oscillations corresponds to the orthogonal cross-sectional area of the FS (A_F) normal to B, which is described by the Onsager relation $F = (\phi_0/2\pi^2)A_F$ [32]. Here, $\phi_0 = 2.07 \times 10^{-15}\,\mathrm{T\,m^2}$ is the single magnetic flux quantum. Thus, $A_F \sim 2.02 \times 10^{-3}$, 3.07×10^{-3}, and $3.50 \times 10^{-3}\,\mathrm{\AA^{-2}}$ are obtained for F_α, F_β, and F_γ, respectively. Correspondingly, the Fermi wave vector ${k_F}^\alpha \sim 0.025$, ${k_F}^\beta \sim 0.031$, and ${k_F}^\gamma \sim 0.033\,\mathrm{\AA^{-1}}$ are determined by assuming that the FS harbors a circular cross section area, namely $A_F = \pi {k_F}^2$ [49]. Note that the variation of F as a function of angle (φ) (Fig. S2 in the Supplemental Material [47]) suggests that the α and β branches could be derived from the same pocket, and the γ band could be 2D. In Fig. S3, the obtained FS shows multiple sheets with a bipyramidal pocket located at the Γ point and elongated along the k_z. According to the φ dependence of orthogonal cross-sectional area of FS normal to B and calculated $k_F(\sim 0.028\,\mathrm{\AA^{-1}})$ for $B \parallel c$, one can see that this pocket is associated with the α (β) branches, whereas the γ band cannot be well reflected in the FS topology for the time being, which still needs to be validated by further studies.

For a system with arbitrary band dispersions, the amplitude of M oscillations can be described by the LK formula: $\Delta M \propto -B^{1/2} \times R_T \times R_D \times R_S \times \sin[2\pi(F/B - \gamma - \delta)]$ [48], where $R_T = (\lambda T)/\sinh(\lambda T)$, $R_D = \exp(-\lambda T_D)$, and $R_S = \cos(\pi g m^*/2m_e)$ are the damping factors due to the phase smearing effect of T, scattering and spin splitting, respectively. Here, $\lambda = 2\pi^2 k_B m^*/(e\hbar\bar{B}) = 14.69 m^*/\bar{B}$, T_D is the Dingle T, $\hbar$, e, m_e, and $\bar{B}$ are the reduced Planck constant, charge of bare electron, free-electron rest mass, and the average B value where Fourier analysis is performed, respectively [48]. More importantly, the sine function term with a phase factor $-\gamma - \delta$ depicts the periodic ΔM oscillation, in which $\gamma = 1/2 - \phi_B/2\pi$, and δ is an additional phase shift and takes the value of 0 ($\pm 1/8$) for a 2D (3D) case [48]. Figures 4(a) and 4(b) show the fits of normalized oscillation amplitudes as a function of T to the thermal damping factor R_T of the LK formula, from which ${m_\alpha}^* \sim 0.040 m_e$, ${m_\beta}^* \sim 0.047 m_e$, and ${m_\gamma}^* \sim 0.054 m_e$ are determined. Here, $\bar{B} = 2/(1/B_{start} + 1/B_{end}) = 1.75\,\mathrm{T}$ with $B_{start} = 1\,\mathrm{T}$ and $B_{end} = 7\,\mathrm{T}$. This is the same method used in Ref. [48]. Obviously, the quasiparticles' m^* of $ScSn_2$ are comparable to those reported for YSn_2 ($0.023m_e$–$0.082m_e$) [24], $LuSn_2$($0.053m_e$–$0.072m_e$) [49], Cd_3As_2($0.044m_e$) [50], $Sr_{1-y}Mn_{1-z}Sb_2$($0.04m_e$–$0.05m_e$) [54], $CaMnSb_2$ ($0.05m_e$–$0.06m_e$) [9], and TaAs ($0.01m_e$–$0.057m_e$) [55], but much lighter than those in MoP ($0.3m_e$–$1.12m_e$) [56], $PtBi_2$($0.64m_e$–$0.68m_e$) [51], and so on. Note that for $ScSn_2$, $\hbar w_c = \hbar eB/m^* \sim 20.22\,\mathrm{meV}$, and $k_B T = 0.17\,\mathrm{meV}$ at 2 K and 7 T. Thus, the condition $\hbar w_c \gg k_B T$ is satisfied and quantum oscillations occur [57]. Since nearly zero m^* is a characteristic feature of Dirac fermions [39], ultrahigh μ could be expected in $ScSn_2$. It is indeed the case that the

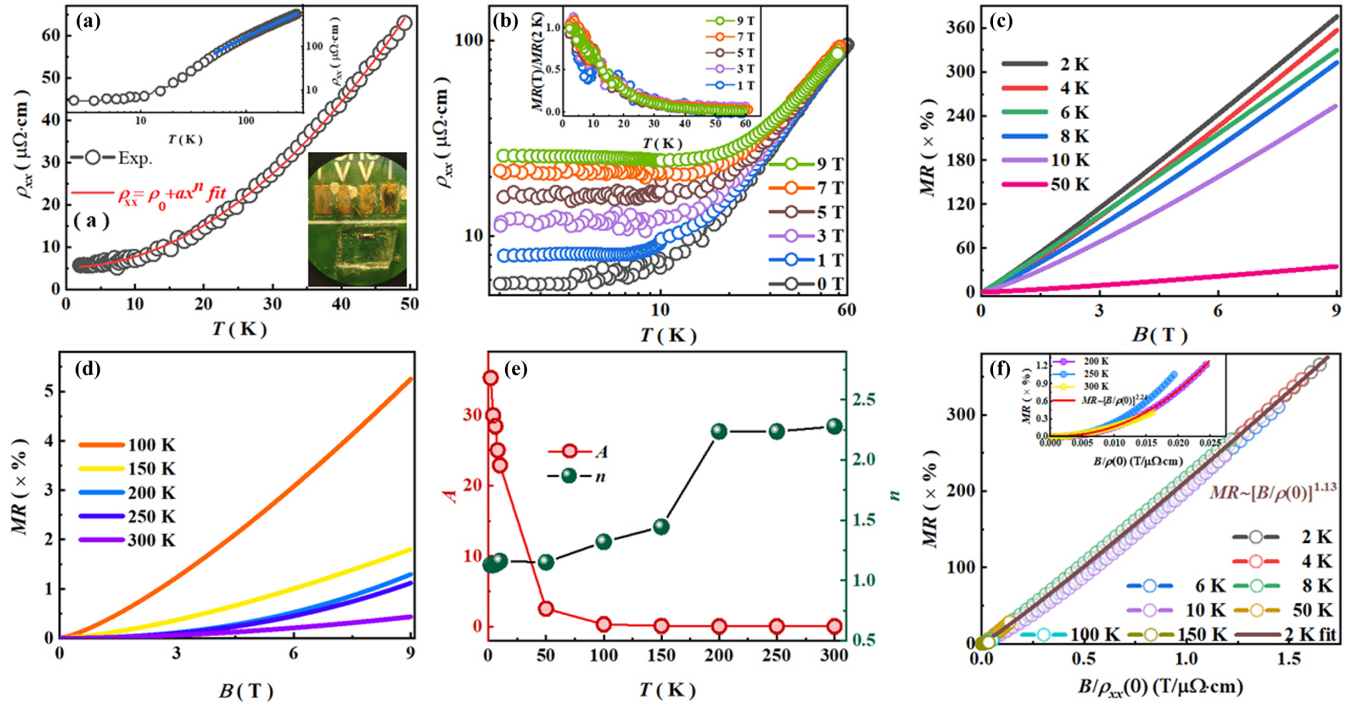

FIG. 5. (a) Low-T ρ_{xx} and its fit with $\rho_{xx} = \rho_0 + ax^n$ ($\rho_0 = 5.22\,\mu\Omega\,\text{cm}$, $a = 0.03\,\mu\Omega\,\text{cm}\,\text{K}^{-n}$, and $n = 1.98$). The upper left inset shows ρ_{xx} as a function of T from 2 to 300 K, where the blue line denotes a linear T dependence. The lower right inset displays the actual device for ρ_{xx} measurements. (b) ρ_{xx} vs T between 2 and 60 K under different Bs. The inset shows normalized MR [MR(T)/MR(2 K)] as a function of T under various Bs. (c), (d) MR vs B at different Ts. (e) A (left axis) and n (right axis) as a function of T. Panel (f) and its inset: Kohler's plot at different T using MR $\sim [B/\rho(0)]^{1.3}$ for 2 K $< T <$ 150 K and MR $\sim [B/\rho(0)]^{2.24}$ for 200 K $< T <$ 300 K.

Fermi velocity ($v_F = \hbar k_F/m^*$) are 7.3×10^5, 4.4×10^5, and 9.4×10^5 m/s for the α, β, and γ bands respectively, of which the values are close to those reported in Cd_3As_2 (1.1×10^6 m/s) and NbP (4.8×10^5 m/s) [50,58]. Figure 4(c) exhibits the ΔM, oscillation components ΔM_α and $\Delta M_{2\alpha}$, and $\Delta M_\alpha + \Delta M_{2\alpha}$ as a function of $1/B$ at 1.8 K. Here, ΔM_α and $\Delta M_{2\alpha}$ are contributions from the F_α and $F_{2\alpha}$ branches, which are separated from the total ΔM by using selective F filters [9]. As shown, $\Delta M_\alpha + \Delta M_{2\alpha}$ is nearly in line with ΔM, suggesting that ΔM are mainly contributed by the two oscillation components. The same method has been employed to analyze the M oscillations for $B \parallel ab$, and the total ΔM are found to be composed of $\Delta M_\beta + \Delta M_\gamma$ [Fig. 4(d)]. Figures 4(e) and 4(f) present the Landau fan diagram with the ΔM_α, ΔM_β, and ΔM_γ oscillation minima and maxima assigned as $N - 1/4$ and $N - 3/4$ LL indices, respectively. A similar method has been adopted in Ref. [9]. Linear extrapolation of the plots yields an intercept ~ -0.06 with a slope of 21.12 T for the F_α branch, an intercept ~ -0.08 with a slope of 32.08 T for the F_β branch, and an intercept ~ -0.03 with a slope of 36.4 T for the F_γ branch. These slope values are in excellent agreement with the Fs obtained from FFT analysis ($F_\alpha = 21$ T, $F_\beta = 32$ T, and $F_\gamma = 36.5$ T). According to the Lifshitz-Onsager rule [48], a closed cyclotron orbit of an electron in the momentum space should be quantized as $A_F(\hbar/eB) = 2\pi(n + 1/2 - \beta' - \delta) = 2\pi(n + \gamma - \delta)$ in the presence of B. Here, β' has a value of 0 for the trivial metals with parabolic band dispersions but π for the nontrivial compounds with linear band dispersions [48]. Thus, for a nontrivial system, the parameter $\gamma - \delta$ extracted from the N-axis intercept in the LL index plot should take any value between $-1/8$ and $+1/8$ [48]. As shown in Figs. 4(e) and 4(f), the obtained intercepts are nicely in this range, suggesting that $ScSn_2$ could harbor nontrivial electronic states. Note that $\phi_B \sim \pi$ could not always be viewed as a fingerprint for the nontrivial topology of Fermi pockets, since it depends on the symmetry or position of extremal orbits [59], while our DFT calculations and the early literature [19] consistently support that $ScSn_2$ is a topological semimetal. Therefore, the values of ϕ_B obtained in Figs. 4(e) and 4(f) are believable.

The upper left inset of Fig. 5(a) shows the zero-field ρ_{xx} for $ScSn_2$ as a function of T. As plotted, the in-plane ρ_{xx} exhibits a continuous decrease from 300 K down to 2 K, displaying a metallic feature in the whole T range. Note that an almost linear-T dependence of ρ_{xx} (blue line) is observed in the T interval 300–50 K. Such a case indicates that electron-phonon scatterings govern the transport [32]. Upon further cooling the sample, ρ_{xx} gently changes and reaches 5.7 $\mu\Omega$ cm at 2 K, which yields a residual ρ_{xx} ratio $RRR \sim 97$, attesting to the high quality of our $ScSn_2$ crystals. The main panel of Fig. 5(a) exhibits the in-plane ρ_{xx} between 2 and 50 K and a fit to the power law $\rho_{xx}(T) = \rho_0 + aT^n$ with $\rho_0 = 5.22\,\mu\Omega\,\text{cm}$, $a = 0.03\,\mu\Omega\,\text{cm}\,\text{K}^{-n}$, and $n = 1.98$. The obtained $n \sim 2$ gives a clue that a pure electronic-correlation scattering dominates the low-T transport in $ScSn_2$ [53]. Similar cases are scarcely reported in other topological compounds where the in-plane ρ_{xx} at low T is either weakly dependent on T or in direct

proportion to T^n with $n \geqslant 3$ [48]. Besides, the prefactor a of the T^2 term in $\rho_{xx}(T)$ of $ScSn_2$ should arouse our attention as well. As seen, it is on the same order of magnitude as those reported in $SrMnBi_2$ ($0.019\,\mu\Omega\,cm\,K^{-2}$) [60], $PtBi_2$ ($0.018\,\mu\Omega\,cm\,K^{-2}$) [51], etc. Note that a is inversely proportional to the Fermi T [$T_F = E_F/k_B = \hbar^2(3\pi^2N/V)^{2/3}/2m^*k$ and $a = \hbar(k_B/E_F)^2 l_{quad}/e^2$] [34,61]. Here, l_{quad} is a material-dependent characteristic length that uniquely arises due to a dimensional analysis [61]. Thus, the obtained nearly zero m^*s in $ScSn_2$ can be easily understood. This finding is highly consistent with the results extracted from the M oscillations shown above.

Figure 5(b) plots the in-plane ρ_{xx} as a function of T for $ScSn_2$ under various Bs. An actual device used in our ρ_{xx} measurements is shown in the lower right inset of Fig. 5(a), where the current flows in the ab plane and B is applied in the c axis. As observed, in the presence of B, the low-T in-plane ρ_{xx} is gently enhanced. Here, the ρ_{xx}-T curves are plotted in a logarithmic scale. Generally, the B induced ρ_{xx} enhancement is proposed to be derived from excitonic gap openings in the linear spectrum of Coulomb interacting quasiparticles [62], while in the inset of Fig. 5(b), the normalized MR [MR/MR(2 K)] data collapse into a universal curve, implying that the T-dependent MR remains the same at different Bs [62]. That is to say, the low-T metallic nature has not been altered in the presence of B. Figures 5(c) and 5(d) exhibit MR as a function of B at various Ts for $ScSn_2$. As displayed, all the MR are positive and still show no sign of saturation up to 9 T. Typically, a large MR of 380% is reached at 2 K and 9 T, which is on the same order of magnitude as those of RPtBi (R = Tb, Ho, and Er) series [63], but one or two orders of magnitude smaller than those of MoP_2 [64], RPn (Pn = Sb and Bi) family [32,62], etc. Besides, it is found that all the MR curves can be well described by a simple power law $MR = A \times B^n$ (not shown). As plotted in Fig. 5(e), A monotonously decreases with the increasing T, while n initially increases from 1.1 (2 K) to 1.4 (150 K) and then almost saturates above 200 K. Note that n approximates to 1 at low T, namely the MR shows a quasilinear B dependence, which has been widely observed in Dirac materials [57,65]. In Fig. 2(c), the P_3 band crossing point with nontrivial electronic nature emerges around the FL. Thus, one possibility for the decrease in n with the decreasing T is that Dirac bands come to participate in the transport and consequently the Dirac fermions are likely to exhibit their footprint in the exponent of B-dependent MR reduced from square. To further study the scattering process, Kohler's scaling analysis on the MR data for $ScSn_2$ is also carried out. For a conventional metal, MR can be described as a scaling function of the variable $B/\rho_{xx}(0)$, $MR = F[B/\rho_{xx}(0)]$, where $\rho_{xx}(0)$ is the zero-field ρ_{xx} at a given T. Such a relation follows from the fact that B enters Boltzmann's equation in the combination $B\tau$ and $\rho_{xx}(0)$ is in direct proportion to the scattering rate $1/\tau$ [62]. Here, τ is the mean time between scattering events of conduction electrons. An enhanced B shrinks the orbital length and meanwhile increases $1/\tau$ by the same factor, which keeps $B\tau$ at a constant and states a self-similarity of the electron orbital motion across different length scales [62]. Consequently, the plot of MR vs $B/\rho_{xx}(0)$ at a fixed T is expected to collapse into a universal curve. Of course, violation of this rule often occurs as well, once different scattering mechanisms emerge on different Ts or length scales or when Landau orbit quantization comes into play [62]. As shown in Fig. 5(f), the scaled MR below 150 K falls on the same curve with $MR \sim [B/\rho_{xx}(0)]^{1.3}$, indicating that a single relevant scattering process is dominant in $ScSn_2$ $ScSn_2$, while MR in the inset of Fig. 5(f) deviates from Kohler's rule, which has been widely observed in several topological semimetals, including RPn (Pn = Sb and Bi) series [62], WP_2 [66], $TaAs_2$ [67], and so on, implying that the multiband effect or multiple scattering mechanisms come into play herein.

To extract the information on carrier concentration (n) and mobility (μ) of $ScSn_2$, its ρ_{xy} measurement is performed. The inset of Fig. 6(a) displays the actual device for ρ_{xy} measurements. Figure 6(a) plots ρ_{xy} vs B at several Ts ranging 2–300 K, in which ρ_{xy} shows a nonlinear B dependence, hinting that more than one type of carrier gets involved in the transport [62]. This is consistent with the results of DFT band structure calculations, where several Fermi pockets can be tracked at the FL. For the multiple-carrier conduction in $ScSn_2$ single crystal, a direct fitting of ρ_{xy} to the two-band model is carried out. Figure 5(b) presents the derived carrier densities (n_h and n_e) and mobilities (μ_h and μ_e) as a function of T, in which the former (latter) ones monotonously increase (decrease) with the increasing T. At 2 K, $n_e = 1.09 \times 10^{20}\,cm^{-3}$, $n_h = 0.91 \times 10^{20}\,cm^{-3}$, $\mu_e = 1.02 \times 10^3\,cm^2\,V^{-1}\,s^{-1}$, and $\mu_h = 0.97 \times 10^3\,cm^2\,V^{-1}\,s^{-1}$. One can see that the densities of electrons and holes ($\sim 10^{20}\,cm^{-3}$) are typical concentrations of semimetals.

Next, we try to understand the linear MR effect in $ScSn_2$ single crystals. Generally, linear MR could occur in the polycrystal systems with open FS, which is derived from an average over the combination of open and closed electron trajectories [68]. Clearly, such a physical picture does not work for the linear MR in $ScSn_2$ single crystals. Another viable reason for linear MR is a breakdown of the low-B transport at a simple density-wave quantum critical point [69]. Note that in Figs. 1(g) and 5(a) no signature of this case can be found. Thus, this model is also at odds with the observed linear MR in $ScSn_2$. Besides, Abrikosov proposed a quantum model to account for the linear MR [68]. The quantum model is available for the systems with the electron distribution enters the so-called "quantum limit" [68]. What is more, a key prediction of this model suggests that linear MR should be stable against T as long as the thermal broadening of LLs is smaller than their separation [57,68], which is given by $\hbar\omega_c$. For $ScSn_2$, $\hbar\omega_c$ in 7 T is 232 K, whereas a sharp decline in its MR occurs above ~50 K. Thus, the linear MR in $ScSn_2$ is not of a quantum origin, but a classical effect.

Except for the above-mentioned mechanisms, the classic Parish-Littlewood (PL) model points out that the inhomogeneity in disordered conductors can yield linear ρ_{xx} response to B [68]. Note that in Fig. 1(f) the EDX results suggest that Sc and Sn are homogeneously distributed across the crystal surface, while we cannot rule out the possible inhomogeneity throughout the whole bulk of our samples. Thus, whether this model works for the observed linear MR in $ScSn_2$ or not still need further studies. A key inference coming from this model is that MR should be dominated by either average mobility $\langle\mu\rangle$ or width of mobility distribution $\Delta\mu$ [57,68].

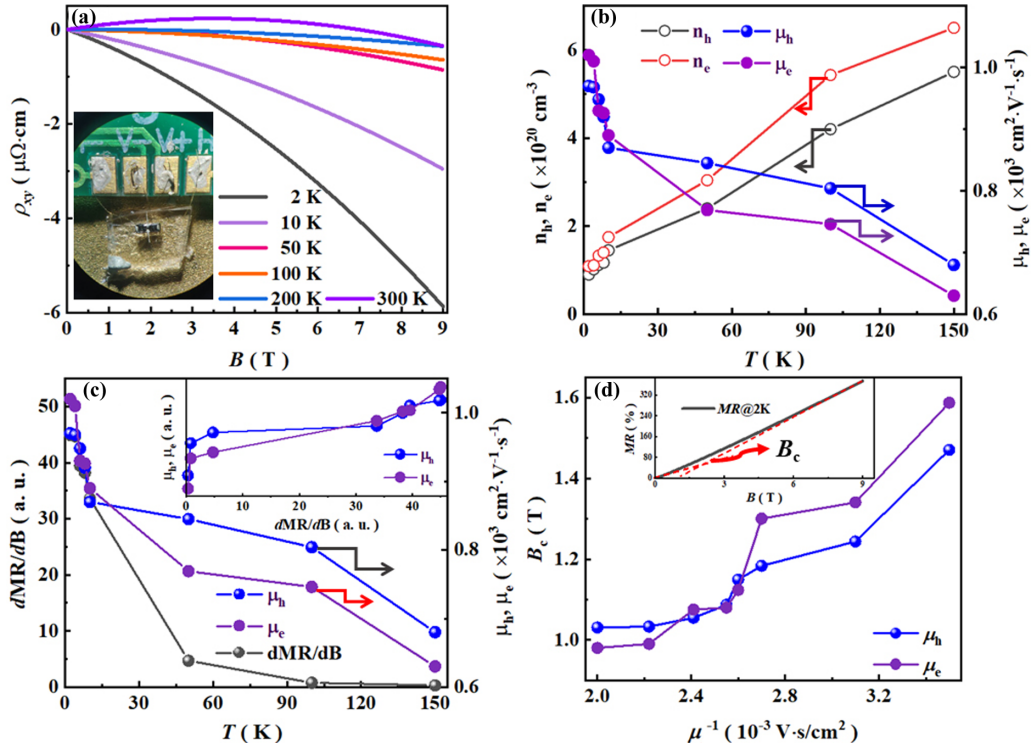

FIG. 6. (a) ρ_{xy} as a function of B at different T for $ScSn_2$. Inset shows the actual device for ρ_{xy} measurements. (b) Evolution of carrier concentrations (n_h and n_e) and mobilities (μ_h and μ_e) as a function of T in $ScSn_2$. (c) High-B dMR/dB (left axis) and μ (right axis) vs T. Inset plots: μ_h and μ_e as a function of dMR/dB. (d) B_c vs μ^{-1}. Inset shows the definition of B_c at 2 K.

For a wide mobility distribution, that is $\Delta\mu > \langle\mu\rangle$, MR is expected to be governed by $\Delta\mu$ [57,68]. $Ag_{2+\delta}Te$ [70], in which $\langle\mu\rangle \sim 0$, shows the $\Delta\mu$-dominated MR. Contrariwise, MR significantly depends on $\langle\mu\rangle$ for a narrow mobility width, i.e., $\Delta\mu < \langle\mu\rangle$ [57,68]. Typically, MR in MnAs-GaAs composite semiconductors is the case [71]. As for $ScSn_2$, it catches our attention that the values of $\mu(\sim 10^3\ cm^2\ V^{-1}\ s^{-1})$ are on the same order of magnitude as the reported results for Bi_2O_2Se nanoplates [72], LuPtSb [73], etc., of which the linear MR is dominated by $\langle\mu\rangle$. Besides, in high-quality $ScSn_2$ crystals, $\Delta\mu$ may be smaller than μ, since the disorder could be partially screened by high n. Thus, the linear MR in our sample cannot be of strong disorder origin. It is reported that in those systems with weak disorders, slopes of the linear portion in MR are always in direct proportion to u [73]. Figure 6(c) exhibits a plot of the first order derivate of MR with respect to B (dMR/dB) at high B [see the left axis] and μ for holes and electrons (see the right axis) as a function of T for $ScSn_2$. As shown, dMR/dB does not seem to have a similar T dependence as those observed in μ_h and μ_e, which is further confirmed by plotting μ_h and μ_e vs dMR/dB in the inset of Fig. 6(c). Besides, an important clue comes from the crossover field (B_c) vs μ^{-1} [73]. Here, we define B_c as the intersection between linear extrapolation of the low- and high-B MR [inset of Fig. 6(d)]. According to the PL model, B_c is expected to show a linear dependence with μ^{-1}, which has been confirmed in MnAs-GaAs composite [71], SiC [74], $PtBi_2$ [75], etc. As shown in Fig. 6(d), B_c varies unlike $1/\mu$, which does not comply with the theoretical expectation and further evidences that the linear MR is not governed by μ. It thus follows that the PL model couldn't be simply employed to understand the linear MR in $ScSn_2$ as well, and the actual mechanism to bring about such a situation is an open question.

V. CONCLUSION

Here, we report the growth of $ScSn_2$ single crystals and study their isothermal M, MR, ρ_{xy}, and so on. The isothermal M along different B orientations show clear quantum oscillations, from which the FS topology with a 3D feature and the quasiparticles with nearly zero m^* and nonzero ϕ_B can be determined, implying that $ScSn_2$ could be a topologically nontrivial material. Besides, B-induced ρ_{xx} enhancement and quasilinear MR are observed at low T. We find that the applied B does not alter the metallic nature of $ScSn_2$, manifesting that the low-T ρ_{xx} upturns are not of a field-induced gap opening origin. Our studying also reveals that the widely reported mechanisms do not work for the observed MR in $ScSn_2$ single crystals, and the exact one to produce the large linear MR is yet to be elucidated.

ACKNOWLEDGMENTS

This work was supported by the Key University Science Research Project of Jiangsu Province (Grant No. 19KJA530003), National Natural Science Foundation of China (Grants No. U1832147 and No. 62005027), Natural Science Foundation of Jiangsu Province (Grant No. BK20181037), and Open Fund of Fujian Provincial Key Laboratory of Quantum Manipulation and New Energy Materials (Grant No. QMNEM1903).

[1] A. A. Burkov, Nat. Mater. **15**, 1145 (2016).
[2] N. P. Armitage, E. J. Mele, and A. Vishwanath, Rev. Mod. Phys. **90**, 015001 (2018).
[3] Z. Wang, Y. Sun, X.-Q. Chen, C. Franchini, G. Xu, H. Weng, X. Dai, and Z. Fang, Phys. Rev. B **85**, 195320 (2012).
[4] Z. K. Liu, B. Zhou, Y. Zhang, Z. J. Wang, H. M. Weng, D. Prabhakaran, S.-K. Mo, Z. X. Shen, Z. Fang, X. Dai, Z. Hussain, and Y. L. Chen, Science **343**, 864 (2014).
[5] H. Weng, C. Fang, Z. Fang, B. A. Bernevig, and X. Dai, Phys. Rev. X **5**, 011029 (2015).
[6] F. Arnold, C. Shekhar, S.-C. Wu, Y. Sun, R. D. dos Reis, N. Kumar, M. Naumann, M. O. Ajeesh, M. Schmidt, A. G. Grushin, J. H. Bardarson, M. Baenitz, D. Sokolov, H. Borrmann, M. Nicklas, C. Felser, E. Hassinger, and B. Yan, Nat. Commun. **7**, 11615 (2016).
[7] H. Huang, J. Liu, D. Vanderbilt, and W. Duan, Phys. Rev. B **93**, 201114(R) (2016).
[8] T.-R. Chang, I. Pletikosic, T. Kong, G. Bian, A. Huang, J. Denlinger, S. K. Kushwaha, B. Sinkovic, H.-T. Jeng, T. Valla, W. Xie, and R. J. Cava, Adv. Sci. **6**, 1800897 (2019).
[9] J. B. He, Y. Fu, L. X. Zhao, H. Liang, D. Chen, Y. M. Leng, X. M. Wang, J. Li, S. Zhang, M. Q. Xue, C. H. Li, P. Zhang, Z. A. Ren, and G. F. Chen, Phys. Rev. B **95**, 045128 (2017).
[10] A. Zhang, C. Liu, C. Yi, G. Zhao, T.-L. Xia, J. Ji, Y. Shi, R. Yu, X. Wang, C. Chen, and Q. Zhang, Nat. Commun. **7**, 13833 (2016).
[11] S. Huang, J. Kim, W. A. Shelton, E. W. Plummer, and R. Jin, Proc. Natl. Acad. Sci. USA **114**, 6256 (2017).
[12] L. Li, K. Wang, D. Graf, L. Wang, A. Wang, and C. Petrovic, Phys. Rev. B **93**, 115141 (2016).
[13] Y. Shiomi, H. Watanabe, H. Masuda, H. Takahashi, Y. Yanase, and S. Ishiwata, Phys. Rev. Lett. **122**, 127207 (2019).
[14] C. Yi, S. Yang, M. Yang, L. Wang, Y. Matsushita, S. Miao, Y. Jiao, J. Cheng, Y. Li, K. Yamaura, Y. Shi, and J. Luo, Phys. Rev. B **96**, 205103 (2017).
[15] J. Y. Liu, J. Hu, D. Graf, T. Zou, M. Zhu, Y. Shi, S. Che, S. M. A. Radmanesh, C. N. Lau, L. Spinu, H. B. Cao, X. Ke, and Z. Q. Mao, Nat. Commun. **8**, 646 (2017).
[16] Y. Yen and G.-Y. Guo, Phys. Rev. B **101**, 064430 (2020).
[17] S. Guan, Y. Liu, Z.-M. Yu, S.-S. Wang, Y. Yao, and S. A. Yang, Phys. Rev. Materials **1**, 054003 (2017).
[18] S. Klemenz, S. Lei, and L. M. Schoop, Annu. Rev. Mater. Res. **49**, 185 (2019).
[19] S. Klemenz, A. K. Hay, S. M. L. Teicher, A. Topp, J. Cano, and L. M. Schoop, J. Am. Chem. Soc. **142**, 6350 (2020).
[20] J. Liu, P. Liu, K. Gordon, E. Emmanouilidou, J. Xing, D. Graf, B. C. Chakoumakos, Y. Wu, H. Cao, D. Dessau, Q. Liu, and N. Ni, Phys. Rev. B **100**, 195123 (2019).
[21] K. Zhao, E. Golias, Q. H. Zhang, M. Krivenkov, A. Jesche, L. Gu, O. Rader, I. I. Mazin, and P. Gegenwart, Phys. Rev. B **97**, 115166 (2018).
[22] A. Wang, S. Baranets, Y. Liu, X. Tong, E. Stavitski, J. Zhang, Y. Chai, W.-G. Yin, S. Bobev, and C. Petrovic, Phys. Rev. Research **2**, 033462 (2020).
[23] M. Pani, P. Manfrinetti, and M. L. Fornasini, Acta Crystallogr. Sect. C **51**, 1725 (1995).
[24] Y. Zhu, T. Zhang, J. Hu, J. Kidd, D. Graf, X. Gui, W. Xie, M. Zhu, X. Ke, H. Cao, Z. Fang, H. Weng, and Z. Mao, Phys. Rev. B **98**, 035117 (2018).
[25] L. L. Zhao, M. S. Mehlman, T. Besara, T. Siegrist, and E. Morosan, J. Magn. Magn. Mater. **341**, 6 (2013).
[26] G. Kresse and D. Joubert, Phys. Rev. B **59**, 1758 (1999).
[27] P. E. Blöchl, Phys. Rev. B **50**, 17953 (1994).
[28] J. P. Perdew, K. Burke, and M. Ernzerhof, Phys. Rev. Lett. **77**, 3865 (1996).
[29] V. I. Anisimov, J. Zaanen, and O. K. Andersen, Phys. Rev. B **44**, 943 (1991).
[30] S. L. Dudarev, G. A. Botton, S. Y. Savrasov, C. J. Humphreys, and A. P. Sutton, Phys. Rev. B **57**, 1505 (1998).
[31] J. Rodríguez-Carvajal, Physica B (Amsterdam, Neth.) **192**, 55 (1993).
[32] H. Gu, F. Tang, Y.-R. Ruan, J.-M. Zhang, R.-J. Tang, W. Zhao, R. Zhao, L. Zhang, Z.-D. Han, B. Qian, X.-F. Jiang, and Y. Fang, Phys. Rev. Materials **4**, 124204 (2020).
[33] R. Sankar, G. Peramaiyan, I. P. Muthuselvam, C. J. Butler, K. Dimitri, M. Neupane, G. N. Rao, M. T. Lin, and F. C. Chou, Sci. Rep. **7**, 40603 (2017).
[34] A. Wang, I. Zaliznyak, W. Ren, L. Wu, D. Graf, V. O. Garlea, J. B. Warren, E. Bozin, Y. Zhu, and C. Petrovic, Phys. Rev. B **94**, 165161 (2016).
[35] Y. Luo, N. J. Ghimire, E. D. Bauer, J. D. Thompson, and F. Ronning, J. Phys.: Condens. Matter **28**, 055502 (2016).
[36] H. Weng, Y. Liang, Q. Xu, R. Yu, Z. Fang, X. Dai, and Y. Kawazoe, Phys. Rev. B **92**, 045108 (2015).
[37] E. Emmanouilidou, B. Shen, X. Deng, T.-R. Chang, A. Shi, G. Kotliar, S.-Y. Xu, and N. Ni, Phys. Rev. B **95**, 245113 (2017).
[38] Q. Xu, R. Yu, Z. Fang, X. Dai, and H. Weng, Phys. Rev. B **95**, 045136 (2017).
[39] J. Hu, Y. L. Zhu, D. Graf, Z. J. Tang, J. Y. Liu, and Z. Q. Mao, Phys. Rev. B **95**, 205134 (2017).
[40] R. Yu, H. Weng, Z. Fang, X. Dai, and X. Hu, Phys. Rev. Lett. **115**, 036807 (2015).
[41] Y. Kim, B. J. Wieder, C. L. Kane, and A. M. Rappe, Phys. Rev. Lett. **115**, 036806 (2015).
[42] Y. Wu, L.-L. Wang, E. Mun, D. D. Johnson, D. Mou, L. Huang, Y. Lee, S. L. Bud'ko, and P. C. Canfield, Nat. Phys. **12**, 667 (2016).
[43] X. Luo, R. C. Xiao, F. C. Chen, J. Yan, Q. L. Pei, Y. Sun, W. J. Lu, P. Tong, Z. G. Sheng, X. B. Zhu, W. H. Song, and Y. P. Sun, Phys. Rev. B **97**, 205132 (2018).
[44] C. Adriano, P. F. S. Rosa, C. B. R. Jesus, J. R. L. Mardegan, T. M. Garitezi, T. Grant, Z. Fisk, D. J. Garcia, A. P. Reyes, P. L. Kuhns, R. R. Urbano, C. Giles, and P. G. Pagliuso, Phys. Rev. B **90**, 235120 (2014).
[45] A. Wang and X. Luo, Compu. Mater. Sci. **194**, 110434 (2021).
[46] J. Noky, Q. Xu, C. Felser, and Y. Sun, Phys. Rev. B **99**, 165117 (2019).
[47] See Supplemental Material at http://link.aps.org/supplemental/10.1103/PhysRevB.104.165128 for validation of nodal loops, φ-dependent M oscillations, and Fs, Fermi surface morphology, which includes Ref. [76].
[48] R. Singha, B. Satpati, and P. Mandal, Sci. Rep. **7**, 6321 (2017).
[49] Y. Zhu, J. Hu, D. Graf, X. Gui, W. Xie, and Z. Mao, Phys. Rev. B **103**, 125109 (2021).
[50] L. P. He, X. C. Hong, J. K. Dong, J. Pan, Z. Zhang, J. Zhang, and S. Y. Li, Phys. Rev. Lett. **113**, 246402 (2014).
[51] W. Gao, N. Hao, F.-W. Zheng, W. Ning, M. Wu, X. Zhu, G. Zheng, J. Zhang, J. Lu, H. Zhang, C. Xi, J. Yang, H. Du, P.

Zhang, Y. Zhang, and M. Tian, Phys. Rev. Lett. **118**, 256601 (2017).

[52] Y. J. Hu, W. C. Yu, K. T. Lai, D. Sun, F. F. Balakirev, W. Zhang, J. Y. Xie, K. Y. Yip, E. I. P. Aulestia, R. Jha, R. Higashinaka, T. D. Matsuda, Y. Yanase, Y. Aoki, and S. K. Goh, Phys. Rev. Lett. **124**, 076402 (2020).

[53] N. Kumar, Y. Sun, N. Xu, K. Manna, M. Yao, V. Süss, I. Leermakers, O. Young, T. Förster, M. Schmidt, H. Borrmann, B. Yan, U. Zeitler, M. Shi, C. Felser, and C. Shekhar, Nat. Commun. **8**, 1642 (2017).

[54] J. Y. Liu, J. Hu, Q. Zhang, D. Graf, H. B. Cao, S. M. A. Radmanesh, D. J. Adams, Y. L. Zhu, G. F. Cheng, X. Liu, W. A. Phelan, J. Wei, M. Jaime, F. Balakirev, D. A. Tennant, J. F. DiTusa, I. Chiorescu, L. Spinu, and Z. Q. Mao, Nat. Mater. **16**, 905 (2017).

[55] F. Arnold, M. Naumann, S.-C. Wu, Y. Sun, M. Schmidt, H. Borrmann, C. Felser, B. Yan, and E. Hassinger, Phys. Rev. Lett. **117**, 146401 (2016).

[56] N. Kumar, Y. Sun, M. Nicklas, S. J. Watzman, O. Young, I. Leermakers, J. Hornung, J. Klotz, J. Gooth, K. Manna, V. Süß, S. N. Guin, T. Förster, M. Schmidt, L. Muechler, B. Yan, P. Werner, W. Schnelle, U. Zeitler, J. Wosnitza, S. S. P. Parkin, C. Felser, and C. Shekhar, Nat. Commun. **10**, 2475 (2019).

[57] M. Novak, S. Sasaki, K. Segawa, and Y. Ando, Phys. Rev. B **91**, 041203(R) (2015).

[58] C. Shekhar, A. K. Nayak, Y. Sun, M. Schmidt, M. Nicklas, I. Leermakers, U. Zeitler, Y. Skourski, J. Wosnitza, Z. Liu, Y. Chen, W. Schnelle, H. Borrmann, Y. Grin, C. Felser, and B. Yan, Nat. Phys. **11**, 645 (2015).

[59] A. Alexandradinata, C. Wang, W. Duan, and L. Glazman, Phys. Rev. X **8**, 011027 (2018).

[60] J. Park, G. Lee, F. Wolff-Fabris, Y. Y. Koh, M. J. Eom, Y. K. Kim, M. A. Farhan, Y. J. Jo, C. Kim, J. H. Shim, and J. S. Kim, Phys. Rev. Lett. **107**, 126402 (2011).

[61] J. Wang, J. Wu, T. Wang, Z. Xu, J. Wu, W. Hu, Z. Ren, S. Liu, K. Behnia, and X. Lin, Nat. Commun. **11**, 3846 (2020).

[62] L.-Y. Fan, F. Tang, W. Z. Meng, W. Zhao, L. Zhang, Z. D. Han, B. Qian, X.-F. Jiang, X. M. Zhang, and Y. Fang, Phys. Rev. B **102**, 104417 (2020).

[63] J. Chen, H. Li, B. Ding, E. Liu, Y. Yao, G. Wu, and W. Wang, Appl. Phys. Lett. **116**, 222403 (2020).

[64] A. Wang, D. Graf, A. Stein, Y. Liu, W. Yin, and C. Petrovic, Phys. Rev. B **96**, 195107 (2017).

[65] K. Wang and C. Petrovic, Appl. Phys. Lett. **101**, 152102 (2012).

[66] A. Wang, D. Graf, Y. Liu, Q. Du, J. Zheng, H. Lei, and C. Petrovic, Phys. Rev. B **96**, 121107(R) (2017).

[67] Z. Yuan, H. Lu, Y. Liu, J. Wang, and S. Jia, Phys. Rev. B **93**, 184405 (2016).

[68] J. Hu and T. F. Rosenbaum, Nat. Mater. **7**, 697 (2008).

[69] K. Wang and C. Petrovic, Phys. Rev. B **86**, 155213 (2012).

[70] M. Lee, T. F. Rosenbaum, M.-L. Saboungi, and H. S. Schnyders, Phys. Rev. Lett. **88**, 066602 (2002).

[71] H. G. Johnson, S. P. Bennett, R. Barua, L. H. Lewis, and D. Heiman, Phys. Rev. B **82**, 085202 (2010).

[72] P. Li, A. Han, C. Zhang, X. He, J. Zhang, D. Zheng, L. Cheng, L.-J. Li, G.-X. Miao, and X.-X. Zhang, ACS Nano **14**, 11319 (2020).

[73] C. Shekhar, S. Ouardi, G. H. Fecher, A. K. Nayak, C. Felser, and E. Ikenaga, Appl. Phys. Lett. **100**, 252109 (2012).

[74] W. J. Wang, K. H. Gao, Z. Q. Li, T. Lin, J. Li, C. Yu, and Z. H. Feng, Appl. Phys. Lett. **105**, 182102 (2014).

[75] X. Yang, H. Bai, Z. Wang, Y. Li, Q. Chen, J. Chen, Y. Li, C. Feng, Y. Zheng, and Zhu-an Xu, Appl. Phys. Lett. **108**, 252401 (2016).

[76] P. Rourke and S. Julian, Comput. Phys. Commun. **183**, 324 (2012).